Nanoscale

PAPER

View Article Online
View Journal

Cite this: DOI: 10.1039/c4nr04069d

Effect of topography on the wetting of nanoscale patterns: experimental and modeling studies†

H.S. Grewal,[a] Il-Joo Cho,[a] Jae-Eung Oh[b] and Eui-Sung Yoon*[a]

We investigated the influence of nanoscale pattern shapes, contours, and surface chemistry on wetting behavior using a combination of experimental and modeling approaches. Among the investigated topographical shapes, re-entrant geometries showed superior performance owing to their ability to restrain the liquid–air interface in accordance with Gibbs criteria. The wetting state is also controlled by the surface texture in addition to the surface chemistry. Topographies with smaller intrinsic angles are better able to support the liquid droplet. Based on these observations, two geometrical relationships for designing superhydrophobic patterns exhibiting the Cassie–Baxter state are proposed. A detailed analysis of the simulation results showed the presence of viscous forces during the initial transient phase of the droplet interaction with the solid surface even at negligible normal velocity, which was verified experimentally using a high-speed imaging technique. During this transient phase, for a polystyrene surface, the liquid front was observed to be moving with a radial velocity of 0.4 m s^{-1}, which gradually decreased to almost zero after 35 ms. We observed that the viscous energy dissipation density is influenced by the surface material and topography and the wetting state. The viscous energy dissipation density is minimal in the case of the Cassie–Baxter state, while it becomes quite significant for the Wenzel state. The viscous effects are reduced for topographies with smooth geometries and surfaces with high slip length.

Received 18th July 2014,
Accepted 22nd October 2014
DOI: 10.1039/c4nr04069d
www.rsc.org/nanoscale

1 Introduction

Wetting is a surface phenomenon involving complex interactions among the participating phases. Both the surface chemistry and topography significantly influence the wetting behavior. Lowering the surface energy helps develop a hydrophobic/omniphobic surface and *vice versa*. In addition to the chemistry, the shape and size of features present on the surface also control wetting.[1] The increase in roughness on both the micro and nanoscale tends to promote the inherent hydrophobic/hydrophilic nature of the surface.[2,3] It helps develop superhydrophobic (apparent contact angle $\theta^* > 150°$ with water) and superhydrophilic surfaces ($\theta^* \approx 0°$). Superhydrophobicity can help reduce drag in micro/nanoelectromechanical systems, submarines, and other submerged machine components such as propellers.[2] It also ameliorates the self-cleaning, anti-fogging, and anti-corrosion properties of surfaces. To obtain superhydrophobic/superhydrophilic surfaces, patterning is normally recommended. The topographical parameters such as shape, pitch, height, and lateral dimensions influence the wetting of patterned surfaces.[4–8] The lotus leaf and the rose petal show the interesting effects of topography on wetting. Mimicking their structures has helped develop superhydrophobic surfaces with low and high adhesion.[9] Similarly, mimicking the surface topography of the shark scale helps reduce the drag coefficient.[10] The unique microstructure on the over-wings of the desert beetle helps collect and deliver water to its mouth.[11] Other species might also have developed similar traits to adapt to the local biosphere.[12] An in-depth understanding of these diversities is required to explore their practical implications. An effective and efficient modeling and simulation tool will definitely help accomplish this task.

In the literature, various different models have been proposed to predict the contact angle and wetting state. Wenzel[13] and Cassie and Baxter[14] modified the classical Young's model to include the real surface microstructure. They concluded that the roughness of the surface and entrapped air significantly influence wetting. Other models have also been proposed to predict the contact angle and wetting state.[15–21] Marmur[22] showed that a Gibbs free energy (GFE) approach can be successfully used in wetting studies. Choi *et al.*[23] showed that modification of the Cassie–Baxter (CB) model is required for enhancing its predictability. Although predicting the wetting state is a challenging task, its knowledge is important to anticipate the rolling angle and contact angle hysteresis.[24,25] The Wenzel state is generally associated with high adhesion,

[a]Center for BioMicrosystems, Korea Institute of Science and Technology, Seoul 136-791, Republic of Korea. E-mail: esyoon@kist.re.kr
[b]School of Mechanical Engineering, Hanyang University, 222 Wangsimni-ro, Seongdong-gu, Seoul 133-791, Republic of Korea
† Electronic supplementary information (ESI) available. See DOI: 10.1039/c4nr04069d

whereas the CB state promotes rolling of the droplet. Bico *et al.*[15] and Quéré[1] proposed a model by equating surface energies associated with Wenzel and CB states to predict the wetting state:

$$\cos\theta_c = \frac{f_s - 1}{r - f_s}, \quad (1)$$

where θ_c is the critical contact angle, f_s is a function of the solid fraction (fraction of the solid surface occluded by the liquid), and r is the roughness parameter (ratio of actual to projected surface area).

Further, using the Gibbs free energy theory, Marmur[22,24] and Tuteja *et al.*[7] proposed modeling approaches that can help predict the contact angle and wetting state of a patterned surface. However, the limitation of this approach (the inability to investigate the influence of the different physical parameters – temperature, velocity of the droplet, and pressure) needs to be addressed. Numerical modeling might help address this limitation. Šikalo *et al.*[26] used the volume of the fluid method to model the effect of a liquid droplet on a flat surface. Their simulation results were in agreement with the experimental data. Ganesan[27,28] used numerical simulations to compare different contact angle models. The lattice Boltzmann method has also shown promising results for chemically and geometrically patterned surfaces.[29–35] However, an approach that can readily model the wetting of different topographical shapes with the required accuracy under a different set of operating conditions is still required. This study aims to fill this gap by investigating the classical finite-element-based numerical simulation technique. We will demonstrate with sufficient experimental and theoretical validation that the finite element method (FEM) can be effectively used to help understand the wetting phenomenon. A detailed analysis helped formulate two simple design constraints to obtain superhydrophobic patterns. The FEM results also showed the presence of a transient stage, preceding the steady state (during static contact angle experiments), supported by high-speed imaging experiments. During this transient stage, dynamic interaction between the liquid droplet and the solid surface gave rise to viscous forces. To demonstrate the versatility of the FEM approach, we also used it to predict the wetting of the egg-beater/crown-shaped structure of the *Salvinia molesta* fern. Owing to the practical limitations imposed by its intricate shape, the wettability of this topography was largely unexplored.

2 Experimental details

In the present work, four types of patterns with different topographies were fabricated using the capillary force lithography technique, and are shown in Fig. 1. Their dimensions and other details are given in the ESI (Table S1†). The detailed fabrication procedure is shown in Fig. S1.† Polyurethane acrylate (PUA) molds were used to fabricate the cylindrical and dome-shaped patterns. These PUA molds were fabricated from Si master molds developed using photolithography and reactive ion etching techniques. The PUA molds were placed on polystyrene (PS) coated Si wafers with a uniform pressure of 20 g cm^{-2}. The PS coating on the Si wafers was obtained using the spin-coating technique followed by heating at 115 °C for 5 min. The cylindrical and dome-shaped patterns were fabricated by controlling the curing temperature during the molding process (Fig. S1†). Hierarchical polymethylmethacrylate (PMMA) patterns were also developed using a similar approach, as shown in Fig. S1.† The curing temperature used in this case was 175 °C (2 h) for microscale structures (Step B) and 120 °C (5 min) for nanoscale features (Step D). The fabrication

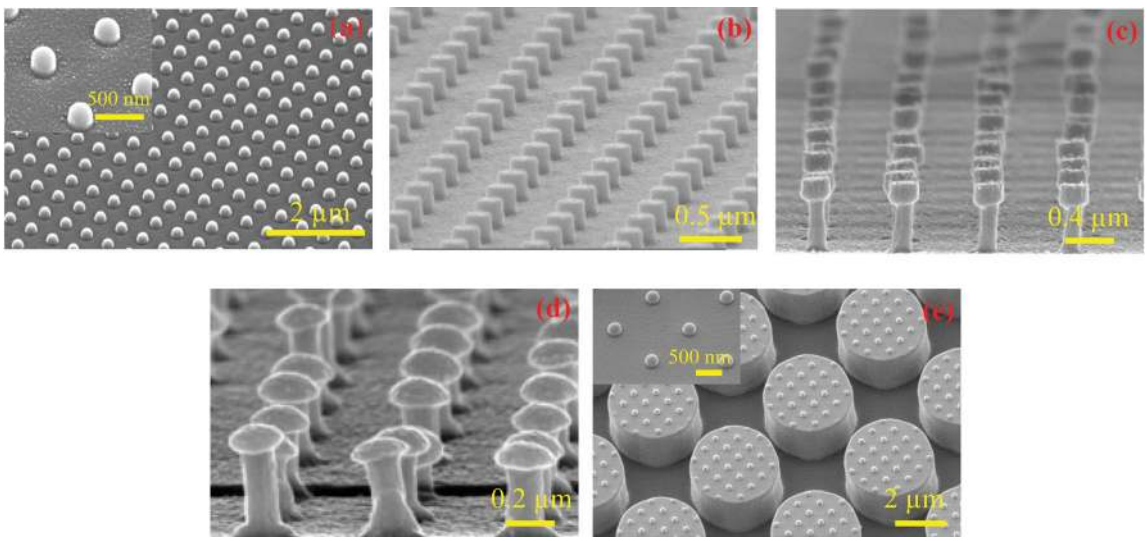

Fig. 1 Scanning electron micrograph showing (a) dome shaped patterns with a magnified image in the inset, (b) cylindrical patterns, (c) mushroom patterns with flat tops, (d) mushroom patterns with round tops and (e) hierarchical patterns with a magnified image in the inset showing the nanoscale features.

details for the mushroom-shaped pattern are also given in Fig. S1.† The fabricated patterns were also coated with a 20 nm thick layer of polytetrafluoroethylene (PTFE) using the C_4F_8 plasma activation method operating at 800 W and 15 Torr pressure. The wetting studies were carried out using the sessile drop method with a 5 μL deionized water droplet and a stabilization time of 5 s for five identical samples.

3 Modeling

3.1 Theoretical modeling

The Gibbs free energy (GFE) approach was used for theoretical modeling of the wetting process. In the GFE approach, the change in the GFE density function was calculated following the procedure (eqn (2)) proposed by Tuteja *et al.*[7] and Bittoun and Marmur:[24]

$$G^* = \frac{\gamma\pi R^2(-2 - 2\cos\theta_t - \sin^2\theta_t(R_\phi f_s\cos\theta_t + f_s - 1))}{4\pi {R_o}^2}, \quad (2a)$$

$$R = R_o\sqrt[3]{\frac{4}{2 - 3\cos\theta_t + \cos^3\theta_t}}. \quad (2b)$$

Here, G^* is the GFE density, γ is the liquid–air surface tension, θ_t is the temporary apparent contact angle, R is the radius of the drop in contact with the surface, R_o is the original radius of the drop at h = 0, where h is the fraction of the pattern height, and R_ϕ is the ratio of the actual wet area to the projected wet area. A code was developed using Matlab 7.10 software wherein the values of θ_t and h were simultaneously varied from 0° to 180° and from 0% to 100%, respectively, in steps of 1° and 1%. This method has been successfully validated by Tuteja *et al.*[7] and is useful for predicting the wetting state and apparent contact angle θ^*. To determine θ^* and the wetting state corresponding to the global energy minimum, θ_t and h were simultaneously varied. Plots showing the variation of the Gibbs energy density function with θ_t and h were prepared for each case. The values of θ_t and h corresponding to the global minimum provide an estimation of θ^* and the wetting state. For $h \approx 0\%$, the CB state exists, while for $h \approx 100\%$, the Wenzel state (fully wetted) exists. In between, the values of h indicate a metastable state.

3.2 Numerical modeling

FEM was used for numerical modeling of the wetting process. An axisymmetric model of the domain of interest was developed using Comsol Multiphysics 4.3a software, as shown in Fig. S2.† The various boundary conditions used for the modeling are shown in Fig. S2.† Fig. S3† shows the meshed domain used for different types of patterned surfaces. Triangular elements with the multiscale meshing scheme were used to discretize the domain. The use of multiscale meshing helped to optimize the computation time and resources. Computational fluid dynamics simulations were performed using the multiphase level set method because of its ability to capture surface tension effects. The level set method is a conventional method used to define the interface between two fluids.[36] In the level set method, eqn (3) is solved in addition to the Navier–Stokes (eqn (4)) and continuity equations (eqn (5)).

$$\frac{\partial\phi}{\partial t} + \nabla(\phi u) + \lambda\left[\left(\nabla\left(\phi(1-\phi)\frac{\nabla\phi}{|\nabla\phi|}\right)\right) - \varepsilon\nabla\cdot\nabla\phi\right] = 0, \quad (3)$$

$$\rho\left(\frac{\partial u}{\partial t} + u\nabla u\right) - \nabla(\mu(\nabla u + \nabla u^{\mathrm{T}})) + \nabla p = F_{st}, \quad (4)$$

$$(\nabla u) = 0. \quad (5)$$

Here, ϕ is the level set function: 1 for air and 0 for the liquid phase. ϕ = 0.5 represents the interface between two fluids. ρ is the density, μ is the dynamic viscosity, ε is the thickness of the transition layer, and λ is the reinitialization parameter. u and p are the velocity and pressure, respectively. F_{st} is the surface tension force, and was calculated using

$$F_{st} = \nabla T, \quad (6)$$

$$T = \gamma(I - (nn)^{\mathrm{T}})\delta. \quad (7)$$

Here, I is the identity matrix, n is the normal to the interface, γ is the surface tension, and δ is the Dirac delta function:

$$\delta = 6|\phi(1-\phi)||\nabla\phi|. \quad (8)$$

A time dependent solver was used and each simulation was run for a total time of 100 ms with a step size equal to 0.1 μs. This time frame was found to be sufficient for the droplet to attain a steady state.

4 Results and discussion

4.1 Wetting state

4.1.1 Modeling and simulation. The wetting states that were predicted using eqn (1), the GFE approach, and the FEM for the different cases (Table S1†) are shown in Table S2.† To identify the wetting states from the FEM results, volume fraction plots were constructed (Fig. 2). In the GFE approach, plots of the Gibbs energy density function ΔG^* with the temporary contact angle θ_t and the fraction of pattern height immersed in water h were used to determine the global energy minima (insets in Fig. 2). The wetting states and contact angle can be determined from these plots, as discussed earlier (section 3.1). Examples of the Wenzel and CB states are shown in Fig. 2a and b, respectively. In the first case, the FEM results show completely submerged cylindrical patterns. The GFE results also show global minima of free energy for 100% intrusion of the liquid corresponding to a contact angle of 125°. In the case of the CB state, the FEM results show the liquid–air interface supported on top of mushroom patterns, complementing the GFE results. The contact angle from the FEM can be estimated from the predicted droplet shapes, which is also shown in the insets in Fig. 2. The experimental and simulated droplet shapes were similar. A metastable state is shown in Fig. 2c. Intrusion of the liquid–air interface was observed. For intrusion depths less than 70%, the metastable state can prevail.[37]

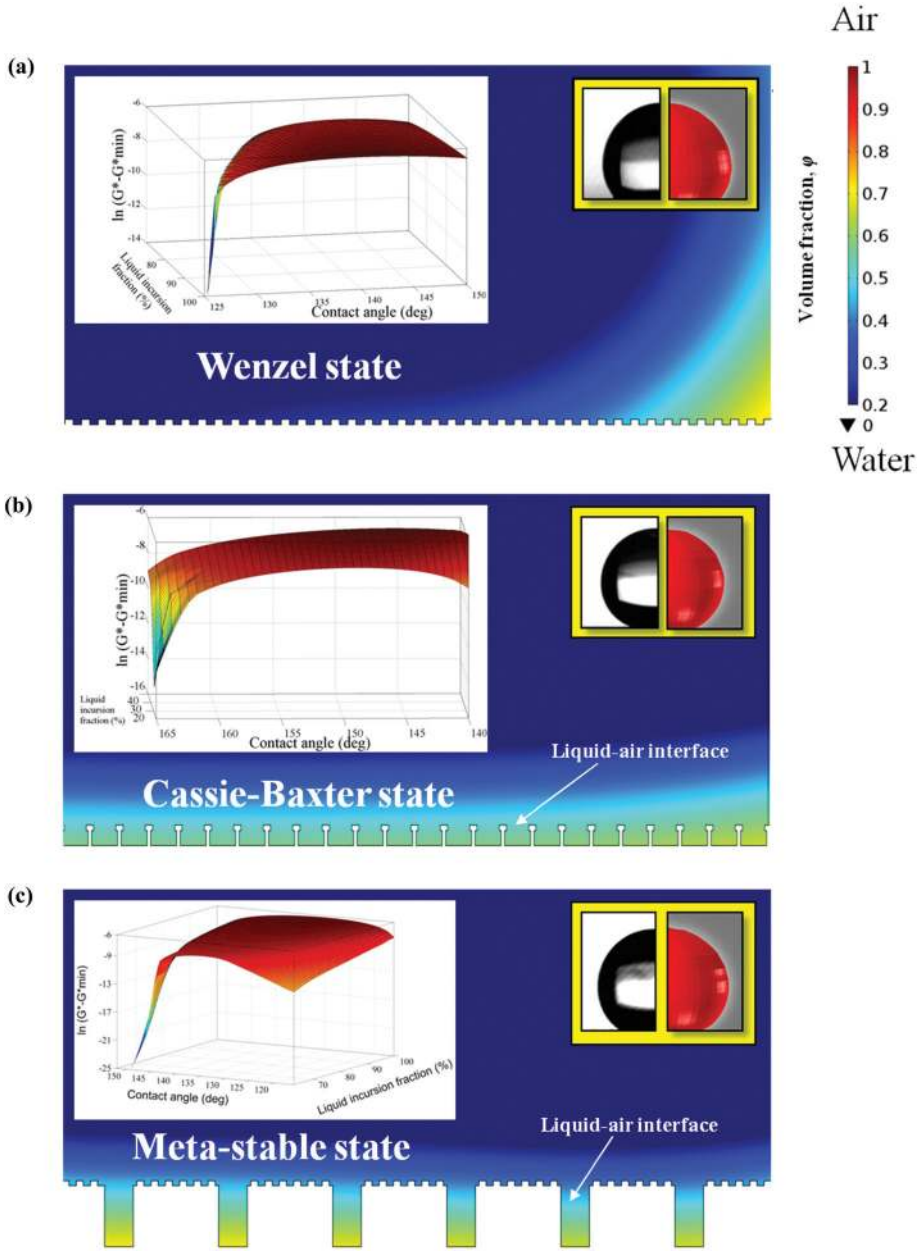

Fig. 2 Wettability states predicted using the finite element method (FEM) and the Gibbs free energy density approach (insets) for (a) cylindrical pillar patterns (pitch = 500 nm) with the PS surface showing the presence of the Wenzel state, (b) mushroom patterns (pitch = 1000 nm) coated with PTFE showing the presence of the Cassie–Baxter state and (c) hierarchical patterns (pitch = 500 nm) coated with PTFE showing the presence of the metastable state. The sky blue line in the volume fraction plots obtained from the FEM corresponds to ϕ = 0.5 and marks the boundary between water and air as shown in the attached color bar. The insets also compare the shapes of the liquid droplets obtained from the experiments and the FEM.

The summary of the results in Table S2† highlights the consistency between the GFE approach and the FEM. Furthermore, in agreement with the GFE approach, the FEM also predicted a transition from the CB to the Wenzel state for PTFE cylindrical patterns, with the increase in pitch P from 500 to 1000 nm (Fig. S4†). This transition occurring at $P \approx 3D$ (diameter) is because of the increased sagging depth of the liquid–air interface (Fig. S5†). The increase in P will increase the sagging of the liquid–air interface supported by adjacent pillars. Furthermore, Quere's model (eqn (1)), although simple in structure, was also able to identify the wetting state with some accuracy. The major drawbacks of this model include the inadequacy to determine the metastable state and the need for experimentally determined θ^*. However, the GFE approach and the FEM are free from such drawbacks and can successfully determine the wetting state.

At this stage, it would be natural to ask about the advantages of the FEM over the GFE approach. A possible answer is

that, compared with the GFE approach, FEM is a versatile tool. It can investigate the influence of different physical parameters (temperature, vibration, velocity, and inclination angles) in addition to different pattern shapes, which is not possible with the present GFE approach. One such example is presented in section 4.4 where we simulate the wetting of *Salvinia molesta* fern using liquids with different surface tensions. The microstructure of *Salvinia molesta* consists of an egg-beater/crown-shaped structure, which helps it to attain a superhydrophobic state because of its air retaining capability.[38] However, such structures are difficult to fabricate, and thus a detailed physical study is yet to be reported.

4.1.2 Effect of topography. Among the different topographical patterns studied in the present work, the re-entrant geometry of the mushroom shape helped it to attain the CB state. The presence of the CB state promotes low contact angle hysteresis and small rolling angle, which are the essential properties of self-cleaning surfaces. The superior performance of the mushroom shape is further evident from Fig. S6.† For this particular simulation, mushroom-shaped patterns were partially removed from the surface. In comparison with cylindrical patterns with similar dimensions, the mushroom-shaped patterns are able to contain the liquid–air interface more efficiently, leading to the CB state. Surfaces with cylindrical patterns are unable to retain the liquid–air interface and become completely submerged (Wenzel state). The results in Fig. S6† again show the robustness and capability of FEM in simulating the wetting process. It successfully differentiated the wetting states depending on the topography.

For the dome and cylindrical patterns, all of the material and pitch combinations showed the Wenzel state, except for the PTFE cylindrical pattern with a spacing factor S_f (ratio of pitch to diameter) of 2. Both the GFE approach and the FEM predicted the CB state for this pattern. The wetting state transformed from the CB to the Wenzel state with increasing S_f, as discussed earlier (section 4.1.1). However, it should be noted that even with similar S_f and r values, the dome-shaped pattern was in the Wenzel state. These patterns also showed lower θ^* compared with cylindrical patterns. For cylindrical patterns, θ^* was almost 10° higher than that for dome-shaped patterns with similar geometrical configurations. This is because of the presence of the Wenzel state for dome-shaped patterns in contrast to CB/metastable states for cylindrical patterns. A difference in θ^* was also observed for mushroom patterns. The round-top patterns showed lower θ^* than flat-top patterns. The above discussion highlights the importance of the surface topography on wetting. The Gibbs criteria[39] of pinning of the liquid–air interface by the sharp edge can explain the difference in the wetting state and θ^* for cylindrical and dome-shaped patterns. As suggested by Tuteja *et al.*,[16] the relationship between the interior angle ψ (Fig. S7†) and Young's contact angle θ is important. For dome-shaped pillars ($\psi = 125°$), $\psi > \theta$ for both PS and PTFE surfaces. As a result, the liquid–air interface is not effectively pinned. However, for cylindrical pillars ($\psi = 90°$), $\psi \sim \theta$ for the PS surface and $\psi < \theta$ for the PTFE surface. The resulting force in this case acts in an upward direction (Fig. S7†) and pins the liquid–air interface at the edge of the cylindrical pattern, leading to the CB state for $S_f = 2$. However, the sagging pressure will dominate with further increasing the S_f, causing bulging of the liquid–air interface and a transition from the CB to the Wenzel state (Fig. S4†). A similar discussion can also explain the performance of round-top mushroom patterns compared with their flat-top counterparts. For hierarchical structures, a metastable wetting state was observed because the liquid was not able to completely penetrate into the microscale structure. The nanoscale structures of hierarchical patterns showed similar behavior to cylindrical patterns. With increasing pitch, and hence for $S_f > 2$, the nanoscale features of the hierarchical structure with the PTFE surface showed a transition from the CB to the Wenzel state.

From the above discussion, we concluded that the geometrical parameters and the shape of the patterns significantly influence the wetting state. The correlation between S_f and the wetting state factor ζ shown in Fig. 3 indicates that a transition to the Wenzel state takes place for $\zeta > 0.75$. The wetting state factor, $\zeta = \left(\left(\sqrt{2}S_f - 1\right)/(2a_r)\right)\tan(\theta_a - \psi)$, is the ratio of sagging height of the liquid–air interface to the height of the pattern geometry, where a_r is the aspect ratio given by H/D and θ_a is the advancing angle. In the case of hydrophobic surfaces, the liquid–air interface is pinned at the top surface of the pattern. With increasing pressure, the angle between the liquid–air interface and the pattern surface increases with a maximum equal to θ_a.[37] With further increasing the pressure, depinning takes place and the liquid–air interface starts moving downward, leading to a transition from the CB state to a metastable state. This phenomenon has been observed

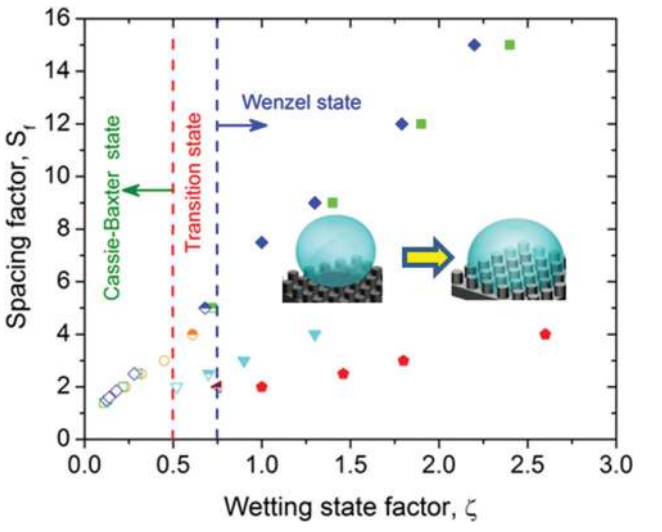

Fig. 3 Plot showing the relationship between the wetting state factor, ζ, and the wetting state for (⬟) dome, (▽) cylinder, (●) mushroom and (◀) micron-sized pillars of hierarchical patterns. The symbols (■) and (◆) represent the experimental results reported by Nosonovsky and Bhushan[40] for cylindrical pillars with D = 5 μm and H = 10 μm and D = 14 μm and H = 30 μm, respectively. The filled symbols represent the Wenzel wetting state, semi-filled symbols represent the metastable state and open symbols represent the Cassie–Baxter state.

experimentally by Lv *et al.*[37] using a laser-type confocal microscope. Lv *et al.*[37] also observed that after 70% displacement of the liquid–air interface, a rapid transition to full wetting or the Wenzel state occurs. The value of ζ calculated for the topographies studied in the present work and cylindrical pattern surfaces (S_f = 1.4–15) with different geometrical parameters reported by Nosonovsky and Bhushan[40] showed similar limiting values. For $\zeta < 0.5$, all patterned surfaces showed the CB state, whereas for $\zeta > 0.75$, the Wenzel state was observed. A metastable or transition state was observed for $0.5 \leq \zeta \leq 0.75$. The value of $\zeta > 1$ indicates that the sagging height of the liquid–air interface is greater than the height of the pattern surface (Wenzel state) (Fig. S5†). This is either due to a large S_f and/or insufficient pinning of the liquid–air interface by topography. To avoid a transition to the Wenzel state it is suggested that either the height of the pattern should be increased (metastable state), the value of S_f should be decreased or the topography should be changed. The influence of topography on ζ can be readily observed in Fig. 3. The dome shaped patterns which had almost similar (in the present work) and/or lower (in the case of Nosonovsky and Bhushan[40]) S_f in comparison with cylindrical patterns had a significantly higher value of ζ. Further, for the same spacing factor, mushroom patterns showed the lowest value of ζ. This indicates the importance of topography in wetting studies. These wetting states predicted by ζ are in agreement with the results of the GFE approach and FEM (Table S2†), as well as the experimental observations of Nosonovsky and Bhushan.[40] According to ζ, to obtain the CB state, S_f should be decreased ($S_f \leq 2$) (Fig. 3) and a_r should be increased. In addition, it is also suggested that the value of θ_a should be increased to enhance the pinning of the liquid–air interface, in accordance with the Gibbs criteria.[39] However, there are practical limitations imposed by the geometrical configuration and material properties. Moreover, the increase in H can only possibly help the transition from the initial Wenzel to the metastable state.

The detailed analysis of the data presented in Fig. 3 and the interpretation of ζ lead to the following two conditions (assuming a_r = 1) that must be satisfied to obtain the CB state:

$$\left.\begin{array}{l} D \geq 0.5P \\ \psi < \theta_a - 26.5^\circ \end{array}\right\} \text{ Topography design constraints for obtaining CB state.}$$

These conditions correspond to $S_f \leq 2$; however, they can be readily modified for other values of S_f. The patterns satisfying these proposed design constraints can exhibit the CB state. These simple design constraints can help in the design of new topographical shapes.

4.2 Contact angle prediction

Comparison of the apparent contact angle θ^* predicted using different analytical models (Table S3†) and the experimental results is shown in Fig. 4a and b. This comparison highlights the inability of these analytical models to accurately predict θ^*. The θ^* values predicted by the GFE approach and the FEM showed remarkable consistency with the experimental observations (Fig. 5). Compared with the analytical models (Table S3†), the FEM and the GFE approach successfully predicted the trend followed by the experimental results, and they captured the effect of pitch on θ^*. Further analysis of these results shows that for all patterns, θ^* decreased with increasing pitch. The transition from the CB/metastable state to the Wenzel state can explain this observation. Patterns in the Wenzel state usually show lower contact angles than those in the CB state,[41] which can be attributed to entrapped air. The entrapped air lowers the free energy of the system, leading to an increase in θ^*. A wetting map (Fig. 6) can help understand the effect of topography and surface chemistry on the wetting state and θ^*. The data from the experimental observations and FEM simulations were used in this map. It shows that patterns in the Wenzel state have lower θ^* than those in the CB state. The increase in pitch leads to a transition in the wetting state because of sagging, as discussed earlier, which results in a decrease of θ^*. Further, from Fig. 6 it can be observed that hierarchical structures with the PMMA surface (θ = 67°) are in the IV quadrant of the wetting diagram by virtue of only topography. This case indicates the importance of topography in attaining the hydrophobic state. Additionally, compared with PTFE hierarchical patterns, the nanoscale pitch of PMMA hierarchical patterns showed a minimal influence on θ^*. Quantitatively, this difference was between 5° and 10°. It is interesting to note that θ^* was abated slightly for hierarchical patterns without nanoscale structures. This may be because of the small protrusion height of the nanoscale structures. However, the nanoscale structures help reduce the overall height of the pattern required for attaining the superhydrophobic state and also decrease contact angle hysteresis (by reducing the wet contact area and forming a tortuous contact line). This can eventually help improve the mechanical integrity of the patterns.[24,42] Probably, hierarchical structures with multiple topographies can readily ameliorate their performance. Mushroom patterns with the PS surface (θ = 92°) exhibited hydrophobicity with θ^* in the range of 115°–135°. The PTFE coating helped mushroom patterns attain the superhydrophobic state with $\theta^* > 160°$ for all pitch values. Therefore, the combined effect of topography and surface chemistry helped mushroom patterns achieve superhydrophobicity. However, topography played a dominant role, because hierarchical structures with similar surface chemistry and considerable height (around 4 times) were only in the hydrophobic regime. Further analysis of the wetting map (Fig. 6) indicates the CB state for patterned surfaces with $\theta > 90°$ and θ^* in the superhydrophobic regime. For surfaces with high contact angles ($\theta \sim 120°$), it is possible to attain the CB state even at $\theta^* \sim 140°$. Below this θ^*, a metastable state with a partially/fully penetrated liquid–air interface will exist depending on the geometrical parameters and topography. Such maps are useful in designing patterns and identifying the wetting state, and can be constructed for other quadrants. Detailed maps explaining the influence of the different geometrical parameters can also be constructed with the aid of FEM.

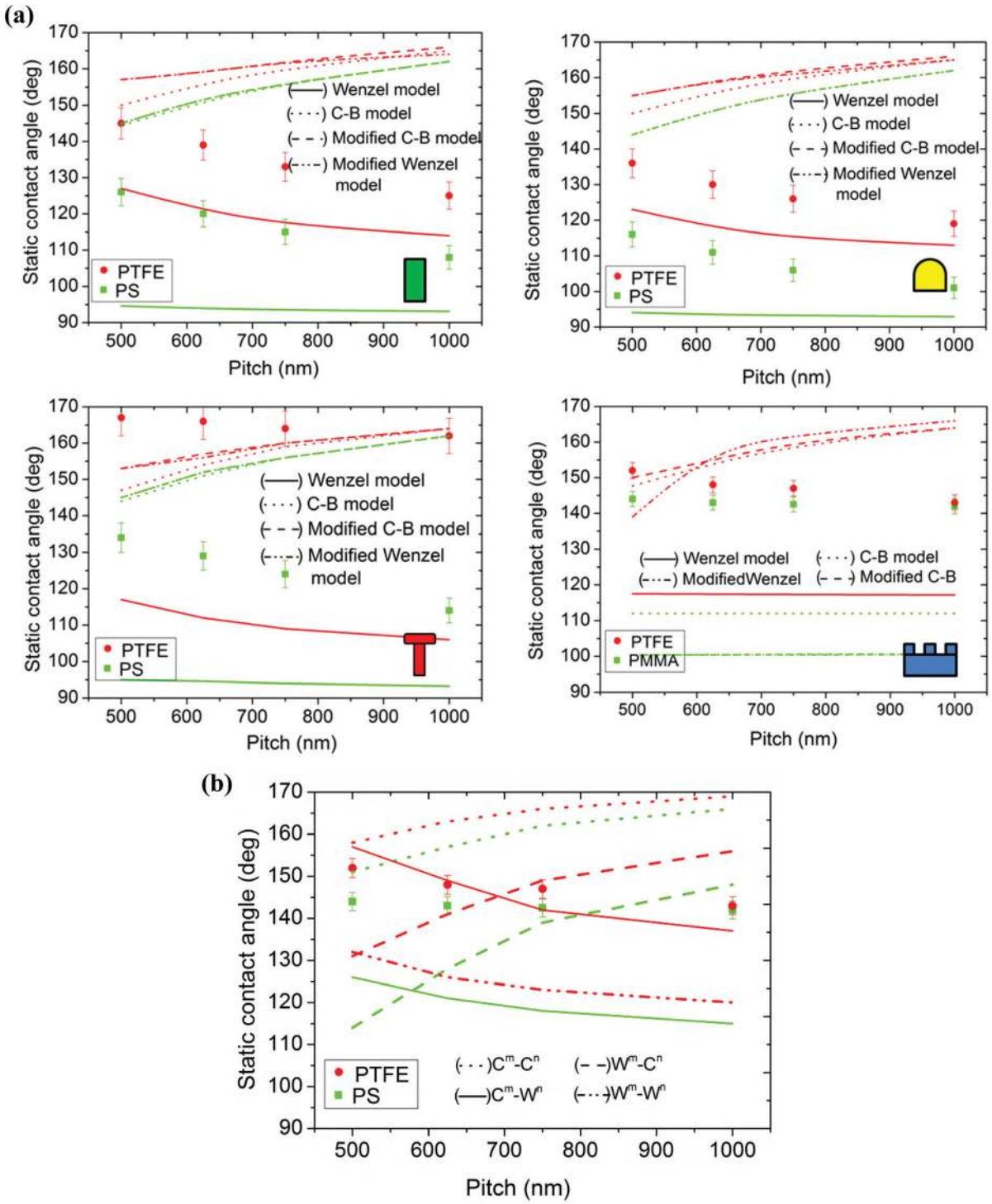

Fig. 4 (a) Plots showing the comparison of the experimental and theoretical values of the contact angle predicted by different analytical models (Table S2†) for the different topographical shapes shown in the insets. (b) Comparison of experimental and predicted contact angles for hierarchical patterns calculated using wetting models suggested by Rahmawan *et al.*[20] (Table S2†).

4.3 Hydrodynamic effects

The apparent contact angle θ^* of all topographies showed direct correlation with S_f (Fig. S8†) for all surfaces (PS, PMMA, and PTFE). A similar correlation was also observed with the actual roughness factor R_ϕ (not shown). This suggests that the confined space in the patterns and the geometrical dimensions are significantly correlated with θ^*. The surface energy and sagging of the liquid–air interface can help explain this correlation. However, for patterns in Wenzel and metastable states, fluid mechanics is also expected to contribute; viscous

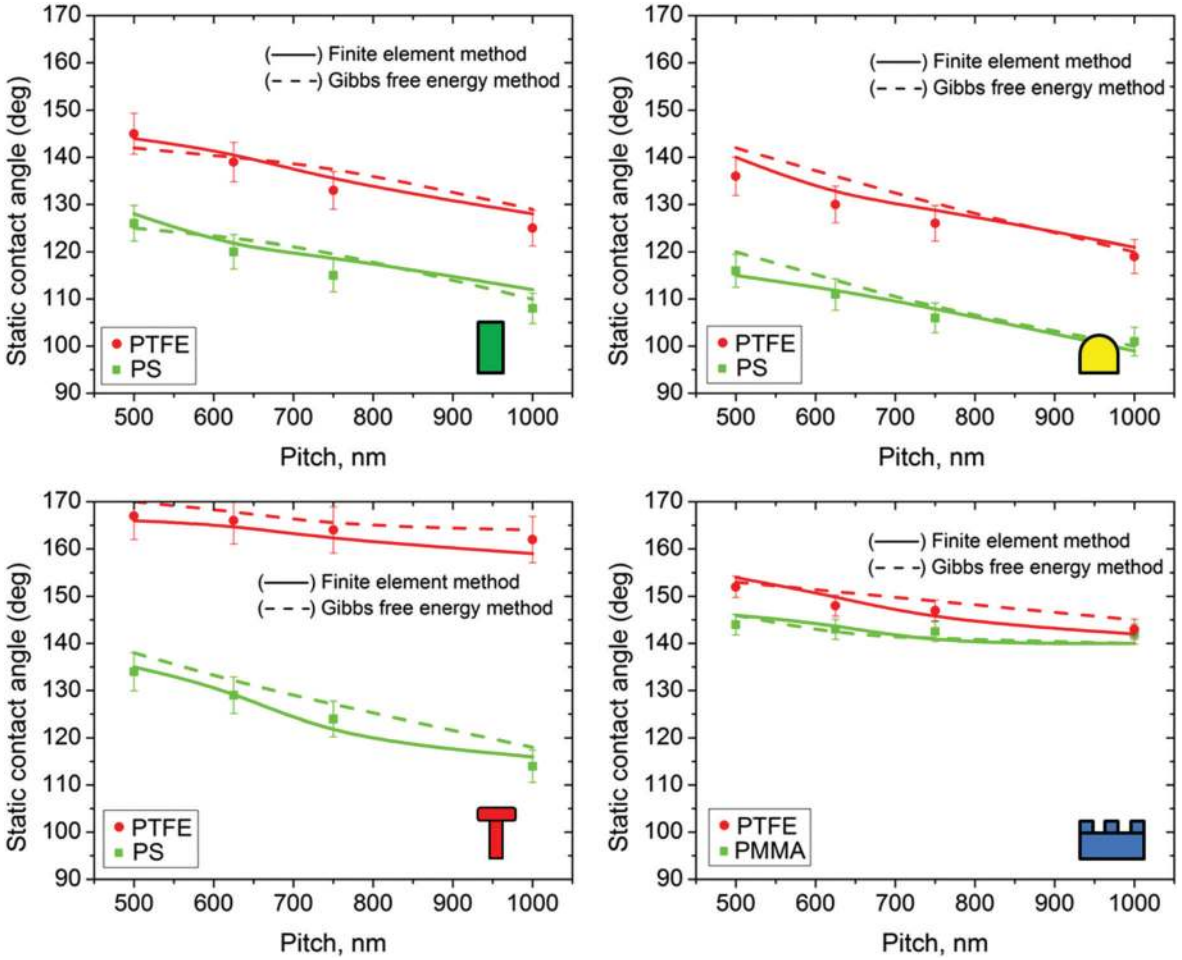

Fig. 5 Contact angles predicted by the Gibbs free energy approach (broken lines) and the finite element method (solid lines) compared with experimental results for the different topographical shapes shown in the insets.

forces will originate during the flow of liquid. According to our hypothesis, the direct correlation of S_f and R_ϕ with θ^* can also be explained by energy dissipation in overcoming the viscous forces arising during the transient state. In between the instance when the droplet comes into contact with the solid surface and attains a steady state, flow of the liquid takes place (adjacent to the solid surface).[43] The images acquired using high-speed photography reported by Vaikuntanathan and Sivakumar[44] also show radial flow of the liquid. The normal velocities in these cases were on the order of 0.29 to 0.97 m s^{-1} and the tangential flow velocity would have been influenced by the normal velocity. However, radial flow of the liquid can still be expected for a drop gently placed on the solid surface. We verified this postulation using a high-speed camera (Photron, IDP Express R2000) operating at 5000 fps with a shutter speed of 0.0001 s. The water drop was gently brought into contact with the flat PS samples held firmly on a movable stage (Movie S1†). The images captured (Fig. S9†) during the droplet and PS surface interaction readily show the presence of a transient state before the drop attains a steady state. During this transient state, rapid movement of the liquid–air interface at a radial velocity (v_r) of 0.4 ± 0.1 m s^{-1} is clearly evident in the initial stage after approximately 13.2 ms of contact. After a lapse of 6.8 ms, the velocity decreased to 0.08 m s^{-1}, and then to almost zero after approximately 22 ms from the time it started moving (13.2 ms). Just prior to this dynamic event, a steady interaction between the water and the solid surface was observed (t = 8–13 ms). During this time, surface tension could be seen to control the wetting process. However, following this stage (t = 13.2 ms), rapid movement of the liquid–air interface relative to the solid surface was observed. Furthermore, a series of pressure waves were seen after this stage. These pressure waves ultimately dissipated because of viscous damping of the liquid (Movie S1†).

During the transient stage, viscous forces will originate because of the relative motion of the liquid with respect to the solid surface and the internal flow of the liquid inside the droplet owing to pressure waves (Movie S2†). These viscous forces will work in combination with surface tension and consume a fraction of the available energy, and can hence influence the contact angle. Keller *et al.*[45] investigated the influence of liquid viscosity on the dynamic contact angle. They reported an increase in dynamic contact angle with viscosity for velocities as low as 20 μm s^{-1}. Recently, Ramiasa

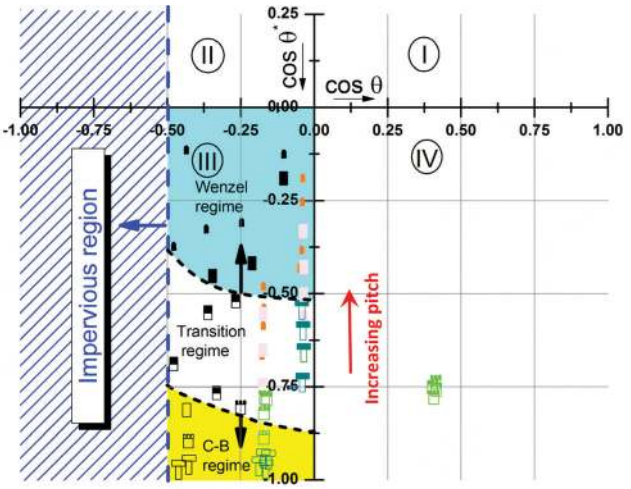

Fig. 6 Wettability map showing the regimes for different wetting states obtained using the experimental and simulation results. The shape of the respective symbols represents the corresponding topography. The filled symbols represent the Wenzel state and open symbols represent the Cassie–Baxter state. The half-filled symbols represent the metastable states. The colored symbols indicate the experimental results of the present study and black symbols indicate the simulation results for imaginary material surfaces (additional simulations were performed to locate the positions of black symbols).

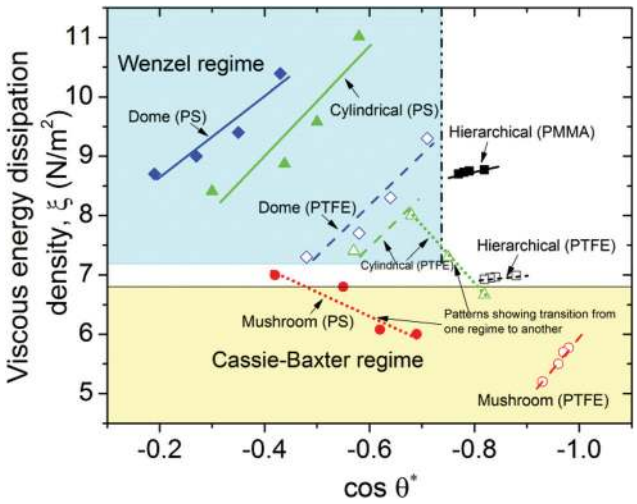

Fig. 7 Correlation between viscous energy dissipation density (ξ) (eqn (3)) and the cosine of the apparent contact angle (θ^*) for different pattern geometries.

et al.[46] also discussed the possibility of viscous forces in liquid droplets. Huh and Scriven,[47] Neogi and Miller,[48,49] and Lopez *et al.*[50] also indicated the presence of viscous effects in liquid droplets in contact with solid surfaces. However, the focus of these investigations was mainly on the dynamic process occurring during the impact of the droplet. Such a dynamic effect can also be observed for the static process.[43] Nevertheless, this dynamic phenomenon exists for a small period of time, although it will still influence the wetting process. The viscous forces, and hence the energy dissipated in overcoming these viscous forces, are directly related to the shear rate $\dot{\gamma}$[51]:

$$W = \int_0^{\tau}\int_{\Omega} \omega \mathrm{d}\Omega \mathrm{d}\tau \approx \mu\left(\frac{v}{l}\right)^2 \Omega\tau. \qquad (9)$$

This expression shows that the energy dissipated because of viscous forces W is directly proportional to the square of $\dot{\gamma}$ (ratio of the velocity v and the characteristic length l). In eqn (9), ω is the energy dissipated because of viscosity, Ω is the volume of the fluid influenced by viscous forces, and τ is the characteristic time. The simulation results also showed the presence of high shear strains adjacent to the patterns. The value of $\dot{\gamma}$ depends on both time and the shape of the pattern (Fig. S10†). From t = 0 (just before the contact of the droplet with the solid surface), the $\dot{\gamma}$ value increased with time until t = 60 ms. With further increase in time, $\dot{\gamma}$ decreased and became almost negligible at t = 100 ms, corresponding to the steady state of the droplet. The results and time frame from this simulation are in agreement with the experimental results. This verifies that the placement of the droplet on the solid surface is a two stage process. After droplet comes in contact with the solid surface and spreads, it undergoes a dynamic state until it attains a steady state. During this transient state, the flow of the liquid occurs in the vicinity of the solid surface. During this flow, viscous forces are generated and consume a portion of the available energy. Therefore, it is important that viscous forces be taken into account in wetting studies. This becomes further evident from Fig. 7, which shows a significant correlation between the viscous energy dissipation density ξ (eqn (10)) and the cosine of the apparent contact angle for different topographical shapes. The ξ value is given by

$$\xi = \frac{4\mu v R_{\phi}}{\delta}\left(\frac{4}{2 - 3\cos\theta + \cos^3\theta}\right)^{2/3}, \qquad (10)$$

and is a function of the dynamic viscosity of the fluid μ, which in the present case is 1.002 cPa s for water, and the Prandtl–Blasius boundary layer thickness δ and R_{ϕ}. The expression for ξ was calculated by dividing eqn (9) by the volume of the droplet and using eqn (2a) to estimate the radius of the contact area of the droplet with the solid surface. The value of R_{ϕ} depends on geometrical parameters and the fraction of pattern height immersed in the liquid, and was calculated from the FEM results. It was found that the material, topography, and wetting state influence the viscous energy dissipation. The value of ξ is smaller for patterns with the PTFE surface than for PMMA and PS patterns. This behavior can be explained based on the slip length. It has been observed that the slip length is directly influenced by θ.[52] PTFE ($\theta \approx 110°$) shows a higher slip length than PS ($\theta \approx 92°$) and hydrophilic PMMA ($\theta \approx 67°$). As a result, the viscous forces are significantly reduced with increasing θ. Other than the material, the topography also controls the magnitude of the viscous forces. The value of ξ is larger for cylindrical patterns than for dome-shaped patterns with identical dimensions. The wetting state is another important factor that affects ξ. Patterns with a CB state have a lower value of ξ than those in the Wenzel state.

For patterns in the Wenzel state, a larger volume of liquid will come into contact with the solid surface. This will eventually increase the resistance to liquid flow, and hence more energy is required to overcome the viscous forces. In addition, the pitch will also influence the magnitude of viscous forces. The viscous forces decrease with the increase of pitch, due to the decrease of shear rate, which has an inverse relationship with the pitch, according to hydrodynamic theory. Therefore, ξ also decreases with the increase of pitch.

It can be concluded from Fig. S9, S10,† and Fig. 7 that viscous forces play an important role in the wetting process and should be taken into consideration. On patterned surfaces, these viscous forces are influenced by the shape, material, and geometrical parameters of the topographical feature.

4.4 Wettability of *Salvinia molesta*

Salvinia molesta is an aquatic fern mostly found in southeastern Brazil. It has leaves with crown-shaped/egg-beater type structures on their surface (Fig. 8a). These structures help it to attain a superhydrophobic state. The crown- or egg-beater-shaped structures shown in Fig. 8a have an intricate shape formed by four lobes emerging from the main stem. Owing to its intricate shape, a three-dimensional (3D) model of the crown structure was used for the FEM simulations. A 3D model of this structure is shown in the inset of Fig. 8a along with the dimensions. Furthermore, a meshed structure of *Salvinia molesta* is also shown in Fig. S11.† The parameters used for the simulation were similar to those used for the other simulations. The material selected for these crown-shaped structures was PTFE with θ = 110°. Two liquids were selected for the simulation: water (γ_{lv} = 72.9 mN m^{-1}) and octane (γ_{lv} = 21.6 mN m^{-1}).

From the plot of the position and shape of the liquid–air interface near the crown patterns (Fig. 8b), the CB state was present for both the liquids. This result is consistent with the practical observation (Fig. 8a) and the results of Barthlott *et al.*[38] The air retaining ability of this complex microstructure aids it in exhibiting superhydrophobicity with the CB state. The value

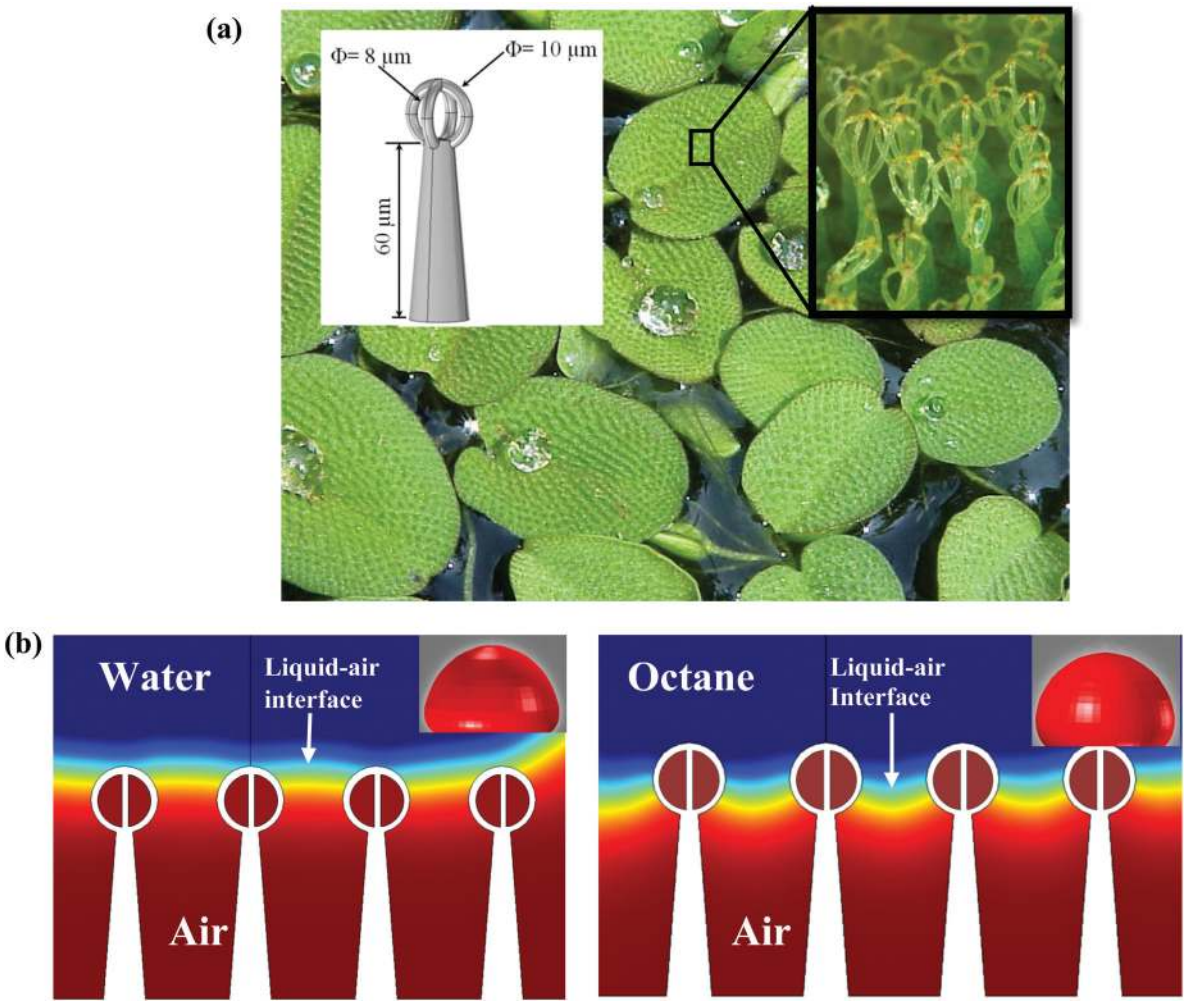

Fig. 8 (a) Water droplets on *Salvinia molesta* leaves (©Barry Rice, sarracenia.com). The inset show the model along with the dimension used for the simulation. (b) Water–air and octane–air interfaces for the droplets. The sky blue color marks the boundary of the liquid–air interface. The inset shows the shape of the liquid droplets on crown-shaped structures.

of θ was found to be 160 ± 3° for water and 135 ± 3° for octane. The water droplet appears to be nicely supported on top of the crown-shaped structures. The liquid–air interface stabilized nearly on top of the crowns leading to an ideal CB state. However, the droplet of octane penetrated into the patterns, and this infiltration was limited to half the height of the crowns (Fig. 8b). The position at which the interface of octane and air got pinned is the position beyond $\psi < \theta$. Therefore, the octane–air interface was not able to penetrate further. As a result, the microstructure of the *Salvinia molesta* fern was able to retain the CB state with the lowest surface energy liquid (octane). These results explicitly demonstrate the ability and effectiveness of the use of FEM in wetting studies. Compared with the lattice Boltzmann method, FEM is a classical tool that is widely used and convenient for wetting studies. Work will be undertaken to study the effect of other factors, such as temperature, velocity, and vibrations, on the wetting of patterned surfaces.

5 Conclusion

The present study showed that the topography along with the surface chemistry and geometrical parameters control the wetting performance of patterned surfaces. Mushroom-shaped patterns with flat tops and PTFE surfaces exhibit superhydrophobicity with water droplets in the ideal CB state. In general, patterns with round tops showed lower contact angles than flat-top patterns. Moreover, the former also showed high affinity for the Wenzel state in accordance with Gibbs criteria. It can be concluded that geometries with intrinsic angle lower than Young's contact angle can exhibit high contact angle with droplets in the CB state owing to their ability to restrain the contact line movement. In addition to the topography, the pitch of patterns also directly influence the contact angle and wetting state. It was observed that with increasing pitch the contact angle decreases along with the transition from the CB to the Wenzel State. Based on these observations, two simple design constraints are proposed that can help select geometrical shapes for obtaining patterns with the CB state. The FEM based numerical simulation technique can help understand the wetting phenomenon. It can aid in designing new patterned surfaces with complex shapes, such as those of *Salvinia molesta* reported for the first time in the present study. With such a powerful tool, the performance of different patterns can be easily evaluated before fabrication, thus saving time and expensive resources. Detailed analysis of FEM simulations showed the presence of viscous forces during the transient stage. During this transient stage, flow of the liquid takes place in a radial direction with respect to the solid surface, giving rise to viscous forces. This hypothesis was validated using a high-speed camera. FEM simulations showed that the topography and other geometrical parameters directly influence the magnitude of these viscous forces.

Acknowledgements

This research was supported by the Korea Institute of Science and Technology (KIST) institutional program (2E24530, 2E25024) and by the Original Technology Research Program for Brain Science through the National Research Foundation of Korea (NRF) funded by the Ministry of Education, Science and Technology (NRF-2012M3C7A1055410). The authors would like to thank Mr Shuxue Piao, KIST, for the experiments. The authors are also grateful to Dr Hyuneui Lim and Dr Seungmuk Ji from the Department of Nature-Inspired Nanoconvergence Systems, Korea Institute of Machinery and Materials, for their help with the high-speed imaging experiments.

References

1 D. Quéré, *Rep. Prog. Phys.*, 2005, **68**, 2495–2532.
2 B. Bhushan and Y. C. Jung, *Prog. Mater. Sci.*, 2011, **56**, 1–108.
3 G. McHale, *Nat. Mater.*, 2007, **6**, 627–628.
4 G. D. Bixler and B. Bhushan, *Nanoscale*, 2014, **6**, 76–96.
5 D. Öner and T. J. McCarthy, *Langmuir*, 2000, **16**, 7777–7782.
6 A. Marmur, *Soft Matter*, 2013, **9**, 7900–7904.
7 A. Tuteja, W. Choi, M. Ma, J. M. Mabry, S. A. Mazzella, G. C. Rutledge, G. H. McKinley and R. E. Cohen, *Science*, 2007, **318**, 1618–1622.
8 D. C. Pham, K. Na, S. Piao, I. J. Cho, K. Y. Jhang and E. S. Yoon, *Nanotechnol.*, 2011, 22.
9 K. Koch, B. Bhushan and W. Barthlott, *Prog. Mater. Sci.*, 2009, **54**, 137–178.
10 G. D. Bixler and B. Bhushan, *Adv. Funct. Mater.*, 2013, **23**, 4507–4528.
11 A. R. Parker and C. R. Lawrence, *Nat.*, 2001, **414**, 33–34.
12 C. Neinhuis and W. Barthlott, *Ann. Bot.*, 1997, **79**, 667–677.
13 R. N. Wenzel, *Ind. Eng. Chem.*, 1936, **28**, 988–994.
14 A. B. D. Cassie and S. Baxter, *Trans. Faraday Soc.*, 1944, **40**, 546–551.
15 J. Bico, U. Thiele and D. Quéré, *Colloid Interface Sci.*, 2002, **206**, 41–46.
16 A. Tuteja, W. Choi, J. M. Mabry, G. H. McKinley and R. E. Cohen, *Proc. Natl. Acad. Sci. U. S. A.*, 2008, **105**, 18200–18205.
17 A. Marmur, *J. Colloid Interface Sci.*, 1992, **148**, 541–550.
18 D. Quéré and P. Aussillous, *Chem. Eng. Technol.*, 2002, **25**, 925–928.
19 Y. C. Jung and B. Bhushan, *Scr. Mater.*, 2007, **57**, 1057–1060.
20 Y. Rahmawan, M. W. Moon, K. S. Kim, K. R. Lee and K. Y. Suh, *Langmuir*, 2010, **26**, 484–491.
21 W. Li and A. Amirfazli, *Adv. Colloid Interface Sci.*, 2007, **132**, 51–68.
22 A. Marmur, *Adv. Colloid Interface Sci.*, 1994, **50**, 121–141.
23 W. Choi, A. Tuteja, J. M. Mabry, R. E. Cohen and G. H. McKinley, *J. Colloid Interface Sci.*, 2009, **339**, 208–216.
24 E. Bittoun and A. Marmur, *Langmuir*, 2012, **28**, 13933–13942.

25 C. Ishino, K. Okumura and D. Quéré, *Europhys. Lett.*, 2004, **68**, 419–425.
26 Š. Šikalo, H. D. Wilhelm, I. V. Roisman, S. Jakirlić and C. Tropea, *Phys. Fluids*, 2005, **17**, 1–13.
27 S. Ganesan and L. Tobiska, *Comput. Visualization Sci.*, 2009, **12**, 329–336.
28 S. Ganesan, *Microfluid. Nanofluid.*, 2013, **14**, 615–625.
29 A. Dupuis and J. M. Yeomans, *Langmuir*, 2005, **21**, 2624–2629.
30 A. Dupuis and J. M. Yeomans, *Europhys. Lett.*, 2006, **75**, 105–111.
31 H. Kusumaatmaja, J. Léopoldès, A. Dupuis and J. M. Yeomans, *Europhys. Lett.*, 2006, **73**, 740–746.
32 A. Kawasaki, J. Onishi, Y. Chen and H. Ohashi, *Comput. Math. Appl.*, 2008, **55**, 1492–1502.
33 X. Jia, J. B. McLaughlin and K. Kontomaris, *Eur. Phys. J.: Spec. Top.*, 2009, **171**, 105–112.
34 R. J. Vrancken, H. Kusumaatmaja, K. Hermans, A. M. Prenen, O. Pierre-Louis, C. W. M. Bastiaansen and D. J. Broer, *Langmuir*, 2010, **26**, 3335–3341.
35 H. P. Jansen, K. Sotthewes, J. Van Swigchem, H. J. W. Zandvliet and E. S. Kooij, *Phys. Rev. E: Stat. Phys., Plasmas, Fluids, Relat. Interdiscip. Top.*, 2013, 88.
36 S. Osher and J. A. Sethian, *J. Comput. Phys.*, 1988, **79**, 12–49.
37 P. Lv, Y. Xue, Y. Shi, H. Lin and H. Duan, *Phys. Rev. Lett.*, 2014, 112.
38 W. Barthlott, T. Schimmel, S. Wiersch, K. Koch, M. Brede, M. Barczewski, S. Walheim, A. Weis, A. Kaltenmaier, A. Leder and H. F. Bohn, *Adv. Mater.*, 2010, **22**, 2325–2328.
39 J. W. Gibbs, H. A. Bumstead and R. G. Van Name, *Scientific Papers of J. Willard Gibbs*, Longmans, Green, 1906.
40 M. Nosonovsky and B. Bhushan, *Nano Lett.*, 2007, **7**, 2633–2637.
41 A. K. Kota, G. Kwon and A. Tuteja, *NPG Asia Mater*, 2014, **6**, 1–16.
42 Y. Yu, Z. H. Zhao and Q. S. Zheng, *Langmuir*, 2007, **23**, 8212–8216.
43 A. L. Biance, C. Clanet and D. Quéré, *Phys. Rev. E: Stat. Phys., Plasmas, Fluids, Relat. Interdiscip. Top.*, 2004, **69**, 163011–163014.
44 V. Vaikuntanathan and D. Sivakumar, *Soft Matter*, 2014, **10**, 2991–3002.
45 A. A. Keller, V. Broje and K. Setty, *J. Pet. Sci. Eng.*, 2007, **58**, 201–206.
46 M. Ramiasa, J. Ralston, R. Fetzer and R. Sedev, *Adv. Colloid Interface Sci.*, 2014, **206**, 275–293.
47 C. Huh and L. E. Scriven, *J. Colloid Interface Sci.*, 1971, **35**, 85–101.
48 P. Neogi and C. A. Miller, *J. Colloid Interface Sci.*, 1982, **86**, 525–538.
49 P. Neogi and C. A. Miller, *J. Colloid Interface Sci.*, 1983, **92**, 338–349.
50 J. Lopez, C. A. Miller and E. Ruckenstein, *J. Colloid Interface Sci.*, 1976, **56**, 460–468.
51 S. Chandra and C. T. Avedisian, *Philos. Trans. R. Soc. London, Ser. A*, 1991, **432**, 13–41.
52 D. Ortiz-Young, H. C. Chiu, S. Kim, K. Voïtchovsky and E. Riedo, *Nat. Commun.*, 2013, 4.

